Discrimination and Quantification of Fe and Ni Abundances in Genesis Solar Wind Implanted Collectors using X-ray Standing Wave Fluorescence Yield Depth Profiling with Internal Referencing

Y. Choi[1], P. Eng[2,3], J. Stubbs[2], S. R. Sutton[2,4*], M. Schmeling[5], I. V. Veryovkin[6] and D. Burnett[7]

[1] X-ray Science Division, Building 431E, 9700 S. Cass Avenue, Advanced Photon Source, Argonne, IL 60439 USA

[2] Center for Advanced Radiation Sources, University of Chicago, Building 434A, 9700 S. Cass Avenue, Argonne, IL 60439 USA

[3] James Franck Institute, University of Chicago, Chicago, Illinois 60439, USA

[4] Department of Geophysical Sciences, 5734 S. Ellis Ave, University of Chicago, Chicago, IL 60637 USA

[5] Department of Chemistry and Biochemistry, 1032 W. Sheridan Rd., Loyola University, Chicago, IL 60660 USA

[6] Department of Chemistry, University of Illinois at Chicago, Chicago, IL 60607 USA

[7] Division of Geological and Planetary Sciences, MS 100-23, California Institute of Technology, Pasadena, CA 91125 USA

* Corresponding author. Email: sutton@cars.uchicago.edu

Submitted to Chemical Geology

May 2016

Abstract

X-ray standing wave fluorescence yield depth profiling was used to determine the solar wind implanted Fe and Ni fluences in a silicon-on-sapphire (SoS) Genesis collector (60326). An internal reference standardization method was developed based on fluorescence from Si and Al in the collector materials. Measured Fe fluence agreed well with that measured previously by us on a sapphire collector (50722) as well as SIMS results by Jurewicz et al. Measured Ni fluence was higher than expected by a factor of two; neither instrumental errors nor solar wind fractionation effects are considered significant perturbations to this value. Impurity Ni within the epitaxial Si layer, if present, could explain the high Ni fluences and therefore needs further investigation. As they stand, these results are consistent with minor temporally-variable Fe and Ni fractionation on the timescale of a year.

Keywords: Solar wind fluence; Genesis mission; x-ray standing wave analysis; depth profile modeling; implant quantification

Introduction

The Genesis spacecraft, launched by NASA in 2001, spent 850 days orbiting the Earth-Sun L1 Lagrange point collecting solar wind by implantation into a variety of pure collector materials, including sapphire, gold, silicon and diamond-like carbon. The mission science goal was to improve the accuracy of chemical and isotopic abundances for the solar photosphere by making solar wind samples available for analysis by sophisticated laboratory instruments. Such improved accuracy is crucial in further developing models of solar evolution and processes.

Although the spacecraft's transport to L1, the solar wind collection activities and its 2004 transit to Earth were highly successful, the reentry vehicle containing the sample return capsule failed to deploy its parachute resulting in a high velocity impact in the Utah desert, fragmentation of the collector wafers and severe contamination of the surfaces of the ultra-pure materials with terrestrial matter. The subsequent challenge has been to nonetheless realize the scientific promise of the Genesis mission by developing analytical techniques designed to allow discrimination between terrestrial surface contamination and implanted solar wind. These efforts have involved development and testing of surface cleaning methodologies followed by application of surface sensitive analytical techniques, such as secondary ion mass spectrometry (SIMS) and resonance ionization mass spectrometry (RIMS). A formidable challenge for the surface cleaning applications is to remove the contamination from the surfaces without affecting the implanted solar wind ions residing at depths on the order of 100 nm,

For quantification of implanted solar wind, SIMS and RIMS are the two surface sensitive techniques that have been applied successfully (e.g., Burnett 2011 and 2013; Heber et al. 2014; Veryovkin et al. 2011). Although these techniques are destructive in that the implanted species plus the collector substrate are sputtered away with the energetic primary ions, the analysis footprint (sputtered crater) is relatively small (~ hundreds of microns) compared to the available area of the collector fragments (~a few mm) thus permitting many independent analyses on the same collectors at different locations. Much of the recent SIMS and RIMS effort has focused on improving analytical reproducibility and accuracy by minimizing sputter depth profiling artifacts originating from ion mixing phenomena (e.g., Sigmund and Gras-Marti 1980).

The purpose of this paper is to describe the application of the x-ray standing wave phenomenon to the non-destructive quantification of solar wind implanted fluences. The x-ray standing wave (XSW) technique at grazing incident angles has been a valuable tool in characterizing the trace element distribution in thin film samples (e.g., Becker et al. 1983, Bloch et al. 1985, Wang et al. 1992, Dev et al. 2000, Templeton et al. 2001, Lee et al. 2006, Gupta et al. 2007, Tiwari et al. 2008, Ghose et al. 2001, Kitts et al. 2009). XSW makes use of the interference between incoming and outgoing grazing x-rays resulting in a nodal pattern of electric field intensity localized perpendicular and near to the surface (Becker et al. 1983; Bloch et al. 1985). By measuring the angular dependence of the fluorescence of the implanted elements and taking advantage of the localized electric field enhancement due to this interference, depth profiles and subsequently quantitative elemental abundance of implanted ions can be determined. An advantage of this method compared to SIMS and RIMS is that depth information extracted from x-ray

reflectivity curves allows the positions of buried structural interfaces to be determined and, therefore, surface contamination to be distinguished from implanted species. A novel aspect of this work is the use of the fluorescence data for a major substrate element as an internal reference for quantification of the other detectible elements.

1 Methodology

1.1 Samples

The flight samples studied in this work were (1) sapphire (Al_2O_3) labeled S50722 and (2) silicon-on-sapphire (SoS) fragment labeled SoS60326, kindly provided by the Genesis Solar Wind Sample Curator (J. Allton) at Johnson Space Center, Houston, TX. The results for the sapphire sample were described by Kitts et al. (2009). This paper will focus on the SoS sample. SoS samples are particularly advantageous for these measurements because the air-silicon and silicon-sapphire interfaces can be readily identified in x-ray reflectivity profiles and therefore provide valuable depth markers for data interpretation (see below).

60326 is a silicon-coated, single sapphire crystal 9.3 mm in length by 22.7 mm wide by 0.7 mm thick, a total solar wind exposed area of 138 mm^2. The silicon coating, ~2000 Å thick, was epitaxially grown on a pre-formed, polished, crystal (Jurewicz et al. 2003). Prior to analysis, 60326 was flushed with ultra-pure water to remove large surface particulates and cleaned in a UV/ozone instrument to remove organic contamination without disturbing the bulk substrate (Calaway et al. 2007); both procedures were performed at the curatorial facility.

In addition to the flight sample, the analysis methodology was applied to two laboratory implantation standards: (1) sapphire (Al_2O_3) flight spare implanted with $2x10^{13}$ $^{56}Fe^+/cm^2$ (courtesy of B. Rout, University of North Texas, Denton, TX), (2) SOS flight spare implanted with $3x10^{13}$ ions/cm^2 of both $^{55}Mn^+$ and $^{60}Ni^+$ at 55 and 60 keV, respectively (Leonard Kroko, Inc, Tustin Ca). The quoted implant fluences for these standards are considered nominal values and significant uncertainties (up to 50%) may exist (Burnett et al. 2015).

1.2 Reflectivity, X-ray Standing Wave, and Fluorescence Yield Measurements

The flight samples and laboratory-implanted spare were analyzed using the Newport General Purpose Diffractometer (Trainor et al. 2006) at the GSECARS sector 13 at the Advanced Photon Source (APS; Argonne National Laboratory). The x-ray beam was derived from an APS undulator with the gap set to supply 11.5 keV photons at the undulator fundamental. A cryogenic Si (111) double-crystal monochromator was used to narrow the energy bandwidth of the beam. A combination of focusing mirrors in a Kirkpatrick-Baez geometry and slits resulted in a 20 x 500 μm (H x V) x-ray beam containing ~ 10^{12} photons/sec. At the grazing incident angles used, the actual footprint of the beam on the sample exceeds 8 mm, representing ~8 x 0.5 mm area over which the XSW measurements average.

The samples and spares were mounted on the diffractometer with the surface normal horizontal and enclosed in a helium-flow sample chamber containing a thin (5 μm) Kapton window. A downstream ionization detector was used to measure the intensity of the reflected x-ray beam. A Vortex ME-4, silicon-drift, energy-dispersive

133 array detector (SII NanoTechnology Inc., now Hitachi High-Technologies Science
134 America, Inc.), mounted with its detector elements parallel to the sample surface, was
135 used to collect XRF spectra as a function of incident angles of the x-ray beam on the
136 sample surface, adjusted using the diffractometer. Silver foil shielding and a custom
137 detector collimator – in direct contact with the Kapton window – were used to limit the
138 detector's view to a restricted area of the sample surface.

139 The critical angle of reflection (θ_C), the maximum angle at which x-rays are
140 reflected from an interface, provides a valuable depth marker. θ_C for both air-silicon and
141 silicon-sapphire interfaces were determined from x-ray reflectivity curves obtained using
142 specular reflection (θ-2θ) trajectory scans with an angular sampling interval of 4
143 millidegrees (θ). Full XRF spectra, collected at each of these angles, form the basis for
144 the quantification of implant fluences.

145 The individual XRF spectra were processed via a peak-fitting routine. The XRF
146 spectra from the four detector elements were averaged and corrected for dead time. The
147 total areas of fluorescence peaks were fit using Gaussian line shapes after subtracting the
148 background. The resulting net fluorescence peak areas were then plotted against incident
149 angle to produce a fluorescence yield profile for each detected element between 1 and 8.8
150 keV. The element responsible for each XRF peak was identified using tabulated energies
151 of electron transitions (Krause and Oliver 1979). For Al and Si, the Kα plus Kβ peaks
152 were used while the Kα peaks were used for all others.

153 **1.3 X-ray Standing Wave Theory**

154 The grazing incidence XSW technique is a combined approach between grazing
155 incidence reflectivity and fluorescence measurements. Specular x-ray reflectivity, with
156 the same incident and reflecting angles, is sensitive to the electron density profile in the
157 sample depth direction. The specular reflectivity can be analyzed using Parratt's (1954)
158 recursive formalism with a depth profile of refractive index *n*. For a fixed incident x-ray
159 wavelength λ, the refractive index at a certain depth position can be written as,

160 $$n = 1 - \delta + i\beta = 1 - \frac{\lambda^2 r_e n_{at}}{2\pi}(f' - if'') \quad (1)$$

161 where r_e is the classical electron radius, n_{at} the atomic density of the element, and f', f'' the
162 real and imaginary parts of atomic scattering factors that depend on λ. δ and β are real
163 and imaginary correction terms to account for dispersion and absorption, respectively.
164 For example, the refractive indices for the Al_2O_3 substrate can be written as,

165 $$n = 1 - \frac{\lambda^2 r_e}{2\pi}[n_{at,Al}(f'_{Al} - if''_{Al}) + n_{at,O}(f'_O - if''_O)] \quad (1a)$$

166 Grazing incidence XSW makes use of the interference between incident and
167 reflected grazing x rays. Near the critical angle of total external reflection [$\theta_C=(2\delta)^{0.5}$],
168 the interference results in enhanced electric field intensity variation localized near the
169 surface. Using parameters obtained from the reflectivity analysis, the corresponding
170 electric field intensity variation can be calculated as a function of x-ray incident angle θ
171 and depth *z* (Parratt 1954, de Boer 1991). X-ray fluorescence intensity modulation
172 depends on the local electric field intensity $|E(\theta, z)|^2 = I_{EF}(\theta, z)$ and depth profile of

fluorescing element concentration $N(z)$. The fluorescence yield Y, normalized to the incident x-ray beam flux, can be written as (Bedzyk et al. 1988, 1989),

$$Y(\theta) = Const \int_{z_{\min}}^{z_{\max}} I_{EF}(\theta, z) N(z) e^{-z/l_a} G(\theta) dz \qquad (2)$$

where l_a (=$\lambda/4\pi\beta$) is the attenuation length of emitted fluorescence. *Const* is an x-ray energy-, element-, and setup-dependent constant, and $G(\theta)$ is a footprint correction factor to account for the x-ray beam footprint change with angle on the sample surface. As seen in the equations above, the fluorescence and reflectivity analysis is based on one dimensional modeling (as a function of z only), thus providing laterally averaged information.

1.4 Substrate Reference Fluorescence

The x-ray fluorescence intensity measured from the major substrate element is used to calibrate the signals from the other trace (implanted) elements. This approach relies on the fact that the substrates are single crystals with well-defined structures and stoichiometries. The number of Al atoms per unit volume in the sapphire substrate, for example, can be readily calculated to be 4.690×10^{22} Al/cm^3. This value is $n_{at,Al}$ in Eq. 1a. The same set of structural parameters from the reflectivity analysis can be applied to the XSW fluorescence analysis. The variable z_{max} in Eq. 2 is the entire substrate thickness, however, for computational simplicity, an appropriate maximum depth z_{max} is chosen, taking advantage of the fact that the incident x-rays fail to penetrate completely through substrate at the small grazing incident angles of interest here.

1.5 Elemental Dependence of Measured Fluorescence Intensities

In order to use the substrate fluorescence for absolute quantification, there are additional factors related to the fluorescence emission and detection processes that need to be added to Eq. 2. Figure 1 summarizes these processes which depend on the incident x-ray energy and element. The detected fluorescence intensities [for example, I(Al-Kα) and I(Fe-Kα) from the Fe:Al_2O_3 sample] are proportional to the incident x-ray intensity

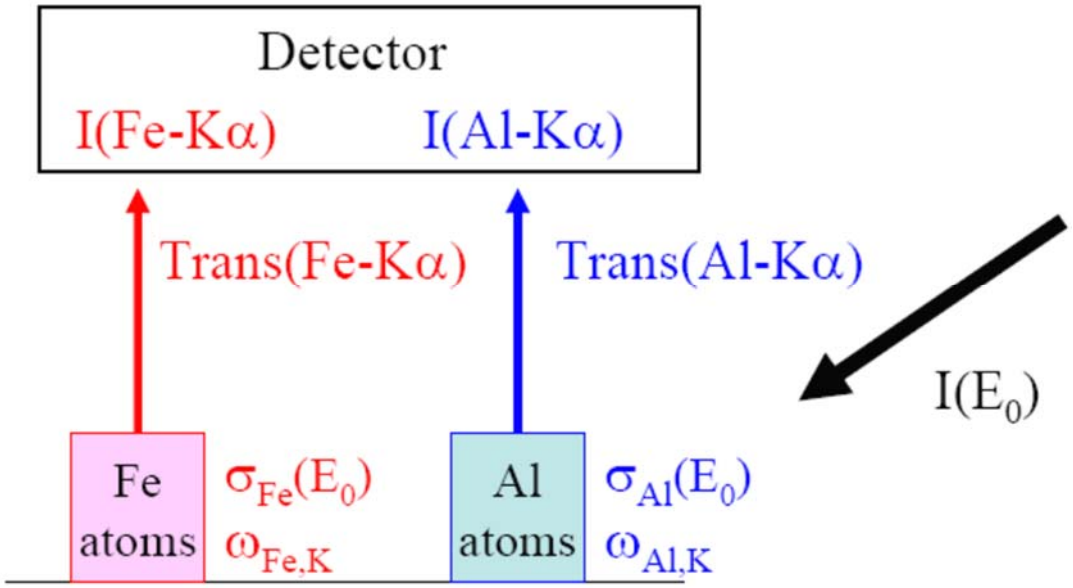

Figure 1: Schematics summarizing the element and energy dependent factors included in the Fe:Al_2O_3 data analysis. $I(E_0)$, I(Al-Kα), and I(Fe-Kα) represent the incident x-ray and measured Al and Fe fluorescence intensities, respectively. σ and ω represent photoelectric cross section at the incident x-ray energy E_0 and fluorescence yield for K fluorescence, respectively. For each fluorescence, *Trans* represents the transmission ratio from the sample surface to the detector, including the detector efficiency at the fluorescence energy. *G* and C_{Geo} represent geometrical factors that are common for the simultaneously measured Al and Fe fluorescence. *G* depends on the sample size, the incident x-ray beam size, and incident angle. C_{Geo} depends on the detector setup.

199 I(E_0), element-dependent photoelectric cross-section $\sigma_{photo\text{-}e}(E_0)$, fluorescence yield ω_K,
200 and transmission ratios between the sample surface and the detector. The absorption of
201 an x-ray by the sample depends on the atom and the incident x-ray energy E_0. This
202 dependence is expressed as the photoelectric cross-section $\sigma_{photo\text{-}e}(E_0)=2r_e\lambda f''$, neglecting
203 small coherent and incoherent scattering cross-section contributions for moderate x-ray
204 energies. Once an atom absorbs an incident x-ray creating an electron hole in the process,
205 the excited atom can relax either by the non-radiative Auger electron process or by the
206 fluorescence emission process. Each element has characteristic fluorescence yields (ω_K)
207 for K-, L-, and M-shells. For example, for K-shell, ω_K quantifies the relative probability
208 for a K fluorescence versus Auger electron emission. Overall, $\sigma_{photo\text{-}e}(E_0)$ (in Barns/atom)
209 and ω_K (unitless) increase as atomic number Z increases, and thus these two factors favor
210 fluorescence emission from high Z elements. These two factors are well tabulated for
211 non-resonant energies (Chantler 1995, 2000; Elam et al. 2002; Krause 1979; McMaster et
212 al. 1969), allowing comparative analysis between fluorescence intensities from trace and
213 substrate elements. The product of these two intrinsic factors is expressed as C_{Int} in the
214 calculations (Table 1). Since each fluorescence yield value describes all the fluorescence
215 lines from a given shell, all the fluorescence lines need to be considered (e.g., ω_K includes
216 $K_{\alpha 1}$, $K_{\alpha 2}$ and K_β). However, in practice, only the most intense lines are measured (e.g.,
217 $K_{\alpha 1}$ and $K_{\alpha 2}$) in which case a correction factor for the transition probability is necessary.
218 Each fluorescence emission has a characteristic energy dependent on the electron
219 energy levels involved, and thus the fluorescence emissions from different elements
220 undergo different degrees of attenuation between the emission point in the sample and the

detector. As mentioned above, the attenuation within the sample is included in Eq. 2. The additional attenuation to the fluorescence detector can be readily determined if the distance and materials between the sample surface and the fluorescence detector are known. The net transmission factor for each Kα fluorescence radiation is expressed as C_{Ext}. In addition, the fluorescence detector efficiency, which depends on fluorescence energy, is included in C_{Ext}. As an example, C_{Int} and C_{Ext} values in the measurements are summarized in Table 1. Taking into account the intrinsic and extrinsic factors mentioned above, *Const* in Eq. 2 now consists of $Const = C_{Int} \times C_{Ext} \times C_{Geo}$, where C_{Int} and C_{Ext} represent intrinsic and extrinsic elemental dependence, respectively. The constant C_{Geo} is an energy-independent geometrical factor accounting for the solid angle of fluorescence detection.

1.6 Depth Profile Modeling

In order to extract the total number of implanted atoms, e.g., determine the solar wind fluence, the measured fluorescence yield profile is fit to equation (2) to obtain N(z) and then N(z) is integrated over depth. The fitting of N(z) is accomplished by assuming a model depth profile and optimizing its magnitude, depth and width. Various depth profiles were attempted and it was found that the total fluence results (proportional to the area under the profile) were quite insensitive to the precise shape of the profile used - indicating that the method is better at determining total fluences than precise implant

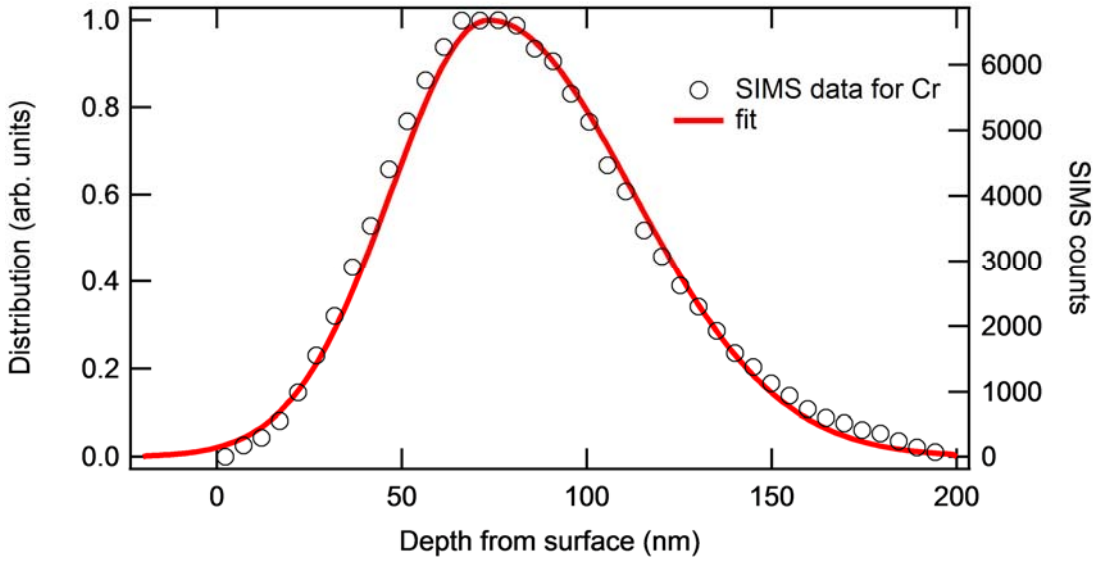

Figure 2: Depth profile used to fit depth distribution of implanted atoms. Points are data for solar wind implanted Cr measured by SIMS. The line is a functional fit to the SIMS data based on an asymmetric Gaussian (see text).

depth distributions.

The principal depth profile used in this work to define the distribution of an implant was that derived from SIMS analysis of solar wind Cr from Genesis flight sample SoS 01863. This asymmetric profile, consisting of 40 discrete measurement points distributed over 200 nm (50 Å/pt), was approximated by an analytical expression produced by two separate Gaussian functions of different widths using the left half of the narrow Gaussian and the right half of the wider one. The approximating function is given by:

$$I(z) = se^{-(z-z_0)/(aw^2)} \qquad (3)$$

where s is a scaling factor, z is depth, z_0 = 720 nm, w is 550 nm and a is an asymmetry factor which is 0.68 for $z<z_0$ and 1 for $z\geq z_0$. Figure 2 shows the comparison between the SIMS data points and this approximating function. In addition to the implant profile, a

253 symmetric Gaussian function was also fit to the fluorescence yield profile to account for

254 “at surface” contamination.

255

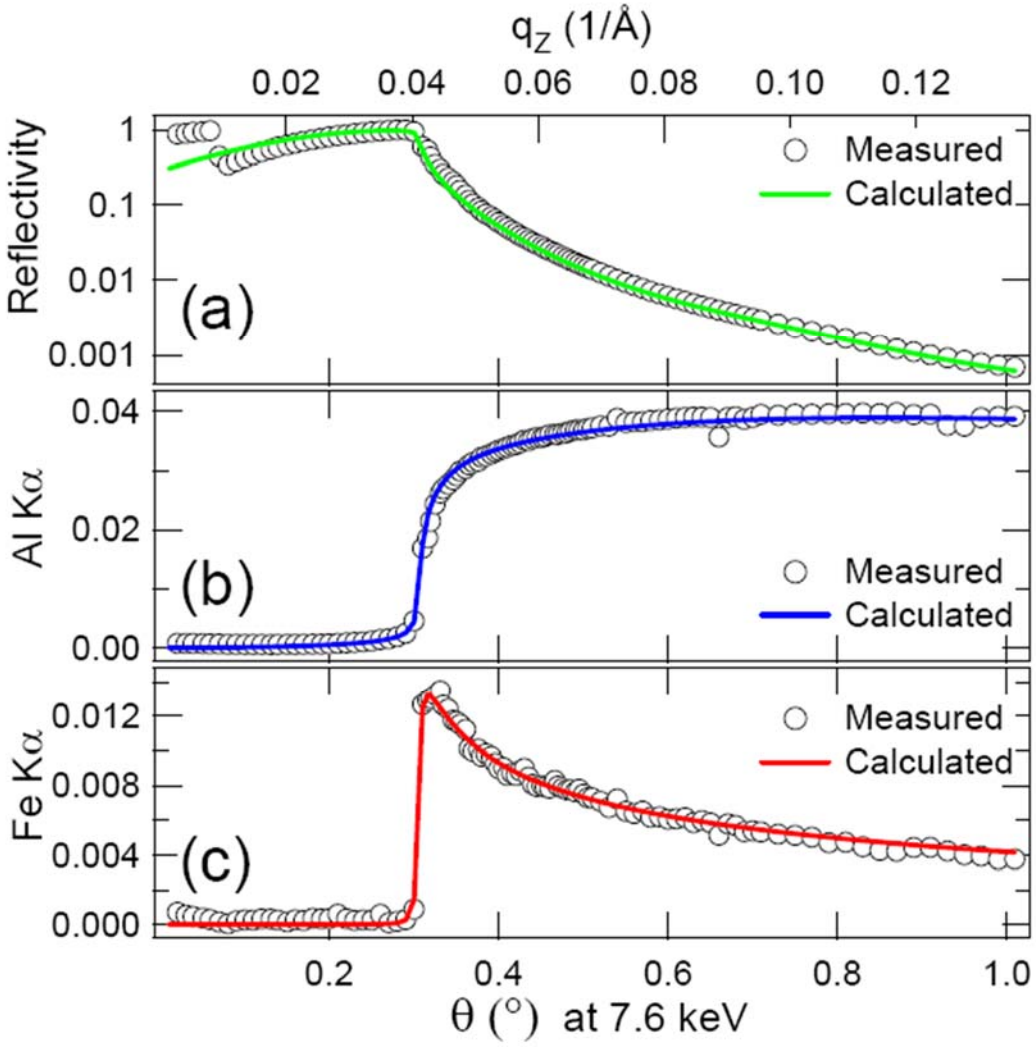

Figure 3: Reflectivity, Al, and Fe fluorescence curves from the Fe:Al_2O_3 sample. Reflected and fluorescence intensities were normalized to the incident x-ray beam flux. (a) Reflectivity. (b) Al Kα. (c) Fe Kα.

256

2 Results

2.1 Fe:Al_2O_3 Implant Standard

Reflectivity and fluorescence curves from the Fe:Al_2O_3 sample are shown in Fig. 3. The substrate density from the reflectivity fit in Figure 3(a) is the same as that of the nominal Al_2O_3 structure, and thus the Al atom distribution $N_{Al}(z)$ can be determined as shown in Figure 4(a). Based on the parameters from the reflectivity, $I_{EF}(\theta, z)$ is calculated. Here the electric field intensity variation is rather simple since there is only one reflecting surface. In the reflectivity and electric field intensity calculations, the presence of the implanted Fe atoms is assumed negligible. This assumption is justified because, even if all of the implanted Fe atoms are confined within a volume of $1cm^2 \times 1Å$, the Fe concentration (2×10^{13} Fe/cm^2Å) is still small compared with the substrate Al concentration (4.690×10^{22} Al/cm^3=4.690×10^{14} Al/cm^2Å). The Al Kα fluorescence curve is fitted by varying C_{Geo} as a scaling factor while using $N_{Al}(z)$ in Figure 4(a), $C_{Int,\ Al\ K\alpha}$ and $C_{Ext,\ Al\ K\alpha}$. The calculated Al Kα fluorescence curve is in good agreement with the measured as shown in Figure 3(b). Once the substrate Al fluorescence is fitted, quantitative analysis of the Fe fluorescence can be done. The Al and Fe fluorescence curves were measured simultaneously so that the C_{Geo} is the same for both. Next, $C_{Int,\ Fe\ K\alpha}$ and $C_{Ext,\ Fe\ K\alpha}$ can be determined since the energies of the incident x-ray and fluorescence emissions are known. Consequently, the only unknown in Eq. 2 is $N_{Fe}(z)$

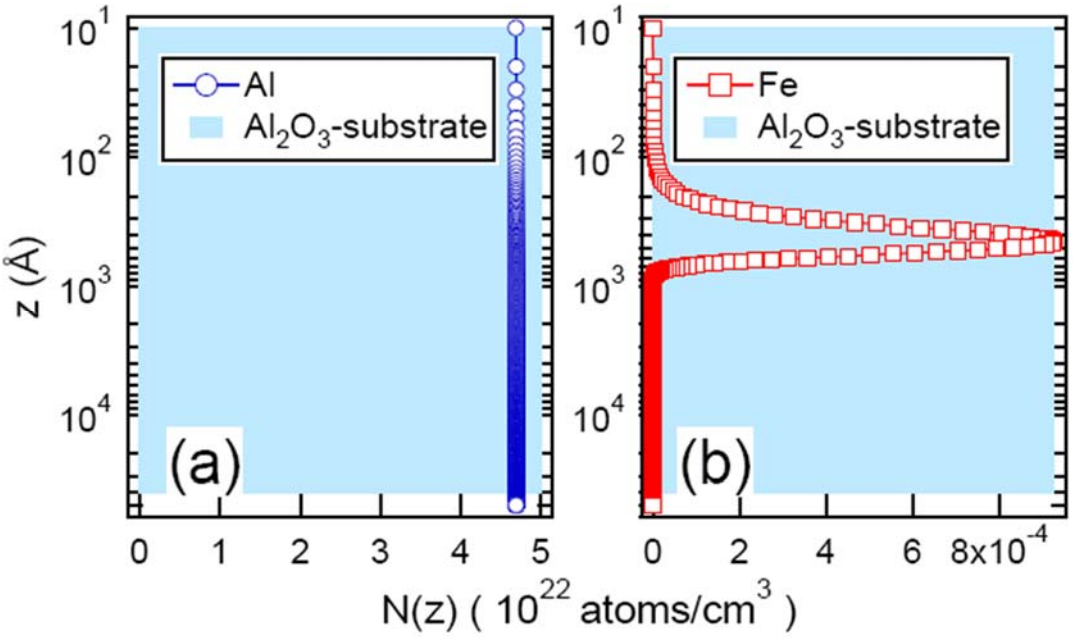

Figure 4: Elemental depth profiles for the Fe:Al_2O_3 sample. (a) Al depth profile obtained from the x-ray reflectivity analysis in Fig. 3(a) and used to calculate the XSW result in Fig. 3(b). (b) Fe depth profile, modeled with a Gaussian peak, to fit the XSW results in Fig. 3(c).

that has the same units as $N_{Al}(z)$. $N_{Fe}(z)$ is modeled with a Gaussian peak, and Figure 4(b) shows fitted $N_{Fe}(z)$ that is centered at 449 Å. The integrated area under the fitted $N_{Fe}(z)$ provides $2.5\pm0.45\times10^{13}$ Fe/cm^2 which is consistent with the nominal value 2×10^{13} Fe/cm^2.

2.2 Mn,Ni:Si:Al_2O_3 Implant Standard

The measured reflectivity curve from the Mn and Ni implanted silicon-on-sapphire (SOS) sample is shown in Figure 5 (black curve). The separate critical angles for the air-silicon interface and the silicon-sapphire interface are clearly observed and define the location of the implant-bearing silicon layer in angle-space unmistakably, i.e., 0.21-0.27 deg. The reflectivity fit (Figure 5, red curve) yielded the structural profile shown in the

Figure 5 inset consisting of: (1) 2.8 nm RMS roughness on the external Si surface, (2) 9.8 nm thick Si layer of density 2.19 g/cm^3 (optimized density and thickness), (3) 267 nm thick Si layer of density 2.33 g/cm^3 and a bulk Al_2O_3 substrate of density 3.97 g/cm^3 (nominal densities assumed). The substrate density agrees well with the nominal sapphire density

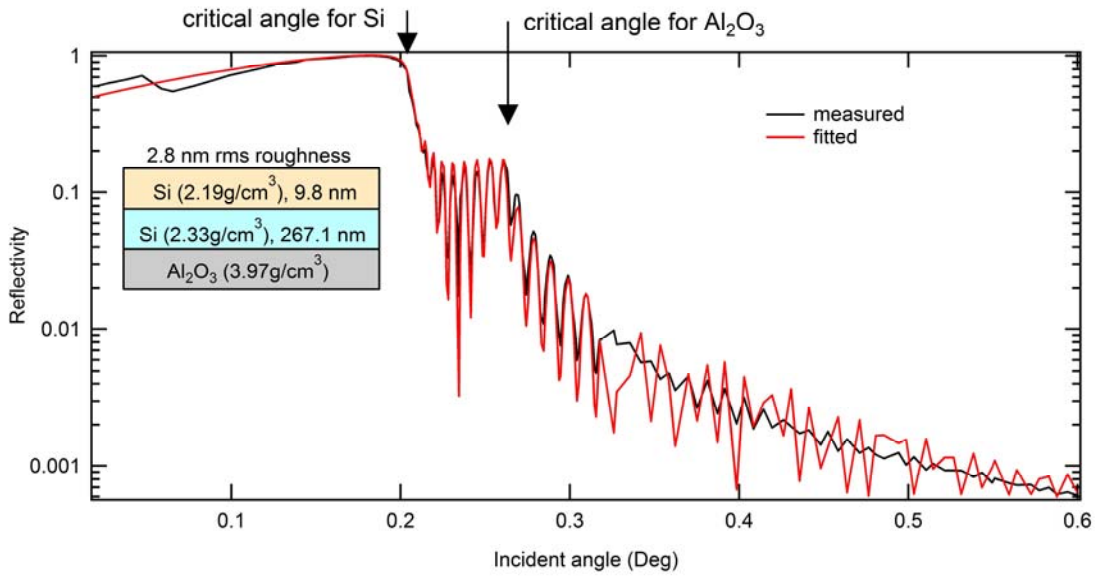

Figure 5: Reflectivity curves from the Mn and Ni implanted silicon-on-sapphire (SOS); measured = black, fitted = red. The separate critical angles for the air-silicon interface and the silicon-sapphire interface are clearly observed and define the location of the implant-bearing silicon layer in angle-space unmistakably, i.e., 0.21-0.27 deg. The reflectivity fit yielded the structural profile shown in the inset consisting of: (1) 2.8 nm RMS roughness on the external Si surface, (2) 9.8 nm thick Si layer of density 2.19 g/ cm^3, (3) 267 nm thick Si layer of density 2.33 g/ cm^3 and a bulk Al_2O_3 substrate of density 3.97 g/ cm^3.

as does the density of the thicker Si layer. The ~10-nm thick, low-density, top layer corresponds to an external oxidized layer of silica, also observed (3.5 nm) by spectroscopic ellipsometry (McNamara and Stansbery 2005). The total Si thickness (277 nm) agrees well with the nominal thickness of 300 nm (Jurewicz et al. 2003).

297 Figs. 6A and 6B show the measured (black curves) and fit (red curves)

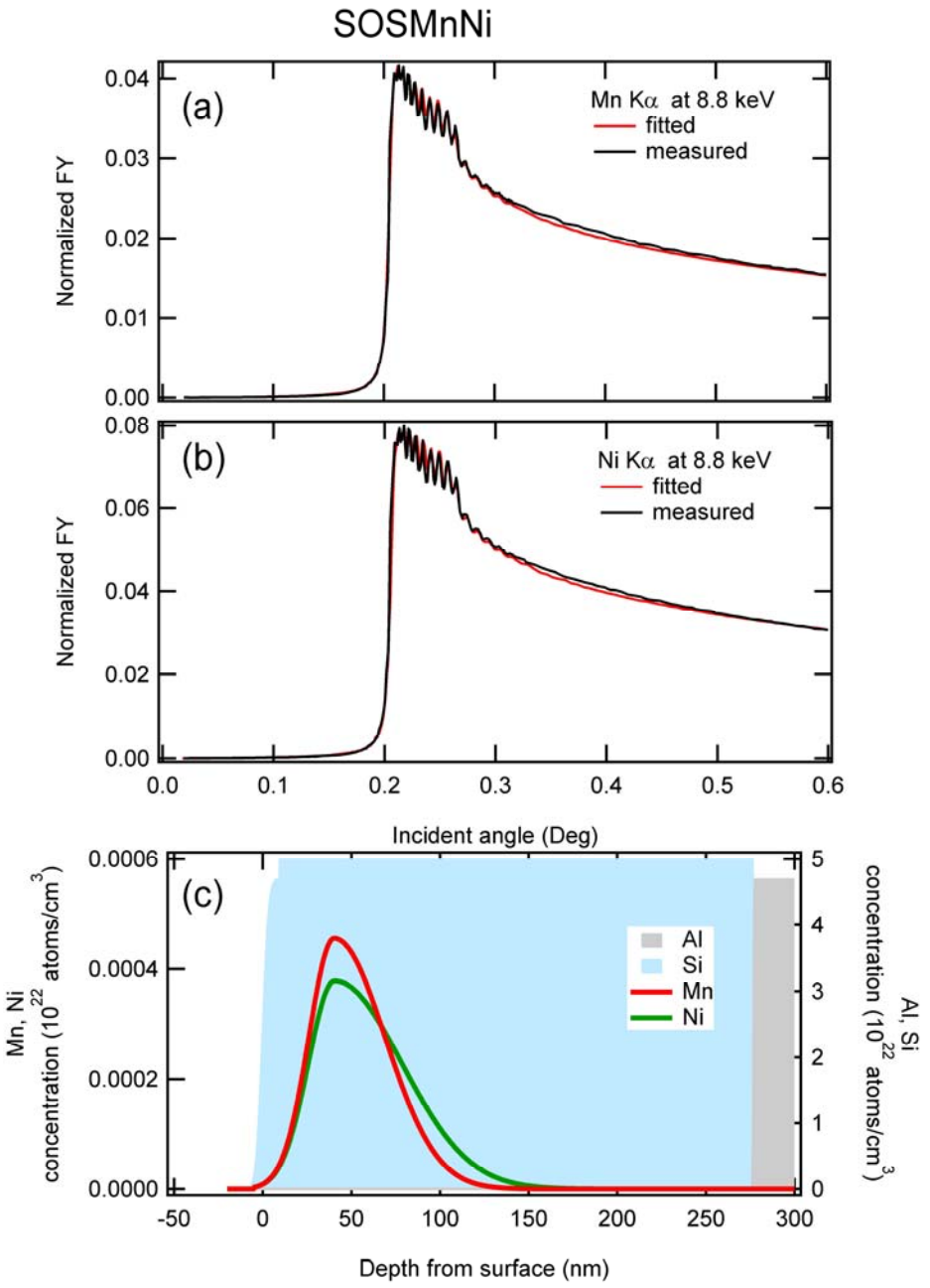

Figure 6: Measured (black curves) and fit (red curves) fluorescence yield profiles for Mn Kα and Ni Kα, A and B, respectively, in the implanted SoS. The sharp rise in both profiles at the air-silicon critical angle (0.21 deg) indicates the high cleanliness of the exterior surface of the silicon layer. Fig. 5c shows the associated depth profile for the four elements obtained with the same approach as for the Fe-implant.

298

fluorescence yield profiles for Mn Kα and Ni Kα, respectively. The sharp rise in both profiles at the air-silicon critical angle (0.21 deg) indicates the high cleanliness of the exterior surface of the silicon layer. Figure 6c shows the associated depth profile for the four elements obtained with the same approach as for the Fe-implant above. The integrated areas under the fitted concentration profiles were $2.50\pm0.23\times10^{13}$ Ni/cm^2 (Figure 5c green curve) and $2.46\pm0.22\times10^{13}$ Mn/cm^2 (Figure 5c red curve) which are both consistent with the nominal values of 3×10^{13} atoms/cm^2. The satisfactory results for the two implants containing Fe in sapphire and Mn and Ni in silicon-on-sapphire demonstrates the robustness of the analytical and modeling approach for determining fluences of implanted species.

2.3 Silicon-on-Sapphire Solar Wind Flight Sample

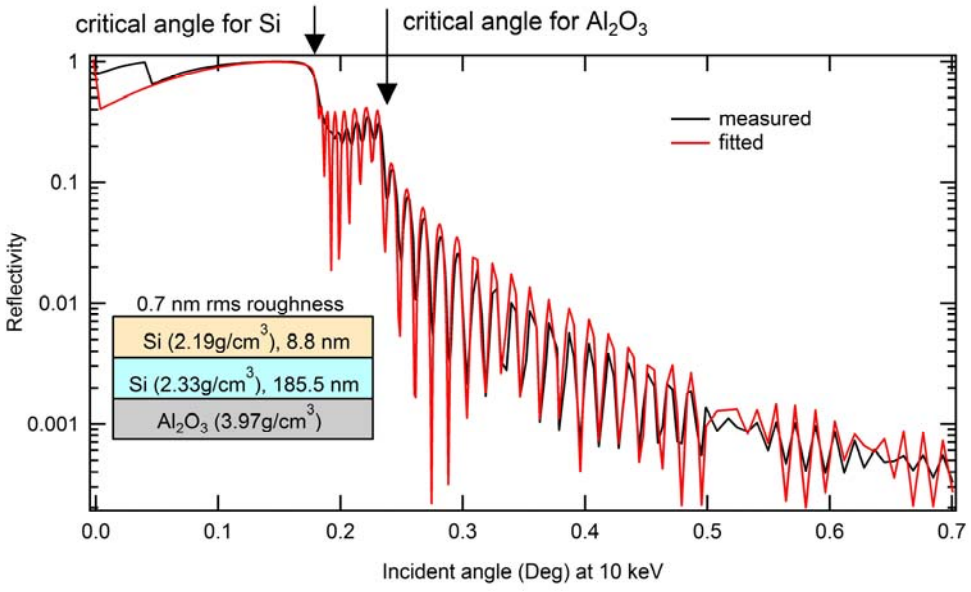

Figure 7: Measured reflectivity curve (black line) and fitted curve (red line) for Genesis flight SoS sample 60326. The optimized structural model is shown in the inset.

311 The internal reference method was applied to determination of solar wind Fe and

312 Ni fluences in Genesis silicon-on-sapphire flight sample SoS60326. Figure 7 plots the

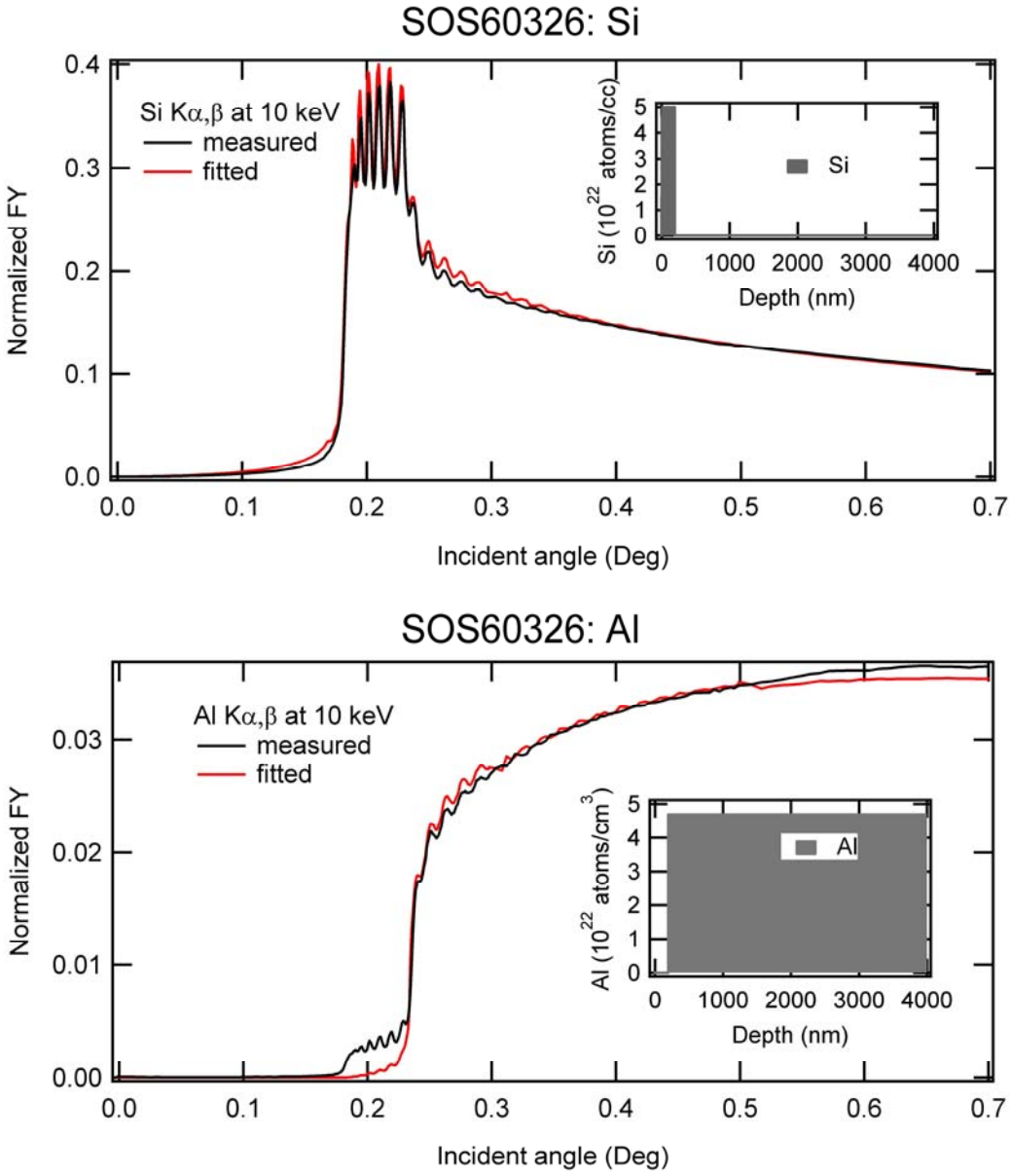

Figure 8: Measured (black) and best-fit (red) fluorescence yield curves for Si (top) and Al (bottom) in flight sample SoS60326. The fits assuming a structure of 200 nm silicon on top of a bulk sapphire substrate agree well with the measurements. These curves provide the internal referencing for obtaining quantitative elemental depth distributions for other elements.

313

measured reflectivity curve (black line) and fitted curve (red line) showing good agreement between the two. The optimized model (inset) indicated 0.7 nm RMS surface roughness on the silicon, an 8.8 nm thick reduced-density silicon layer (density 2.19 g/ cm^3 optimized), a bulk silicon coating layer 185.5 nm thick (density 2.33 g/ cm^3 assumed) and the thick sapphire substrate (density 3.97 g/ cm^3 assumed). The combined silicon layer thickness of 194 nm agrees well with the spectroscopic ellipsometry results on flight SoS wafers which indicated a Si layer of thickness 185 nm (McNamara and Stansbery 2005).

Figure 8 shows the measured (black) and best-fit (red) fluorescence yield curves for Si (top) and Al (bottom) in the flight sample SoS60326. The fits assuming a structure of 200 nm silicon on top of a bulk sapphire substrate agree well with the measurements. These curves provide the internal referencing for obtaining quantitative elemental depth distributions for other elements, notably Fe and Ni.

The top plot in Figure 9 shows the measured (black) and best-fit (red) fluorescence yield curves for Fe. The bottom plot in Figure 9 shows the depth-dependent structure profile for Fe corresponding to the red fit in Figure 9 top. The fit was produced using two components, a Gaussian shaped surface component (Gaussian 1) and an asymmetric Gaussian shaped implant profile (Gaussian 2). The shape of the implant profile was constrained to be that measured by SIMS analysis for chromium as described above (equation 3 and Figure 2). Thus, the modeled depth profile for implanted Fe was constrained in width, asymmetry and depth of the maximum whereas the amplitude was the only variable. This approach assumes the depth distribution for Cr is the same as that

for Fe which is a good assumption here since the integrated fluence results, the main goal of this work, are insensitive to the precise elemental depth distributions.

The results for Fe yield a surface-correlated (contamination) concentration of 4.31 ± 0.40 x 10^{11} Fe atoms/cm^2 above a zone with concentration 1.30 ± 0.12 x 10^{12} Fe atoms/cm^2, the latter being the solar wind implant. The uncertainty in the solar wind fluence was determined from the

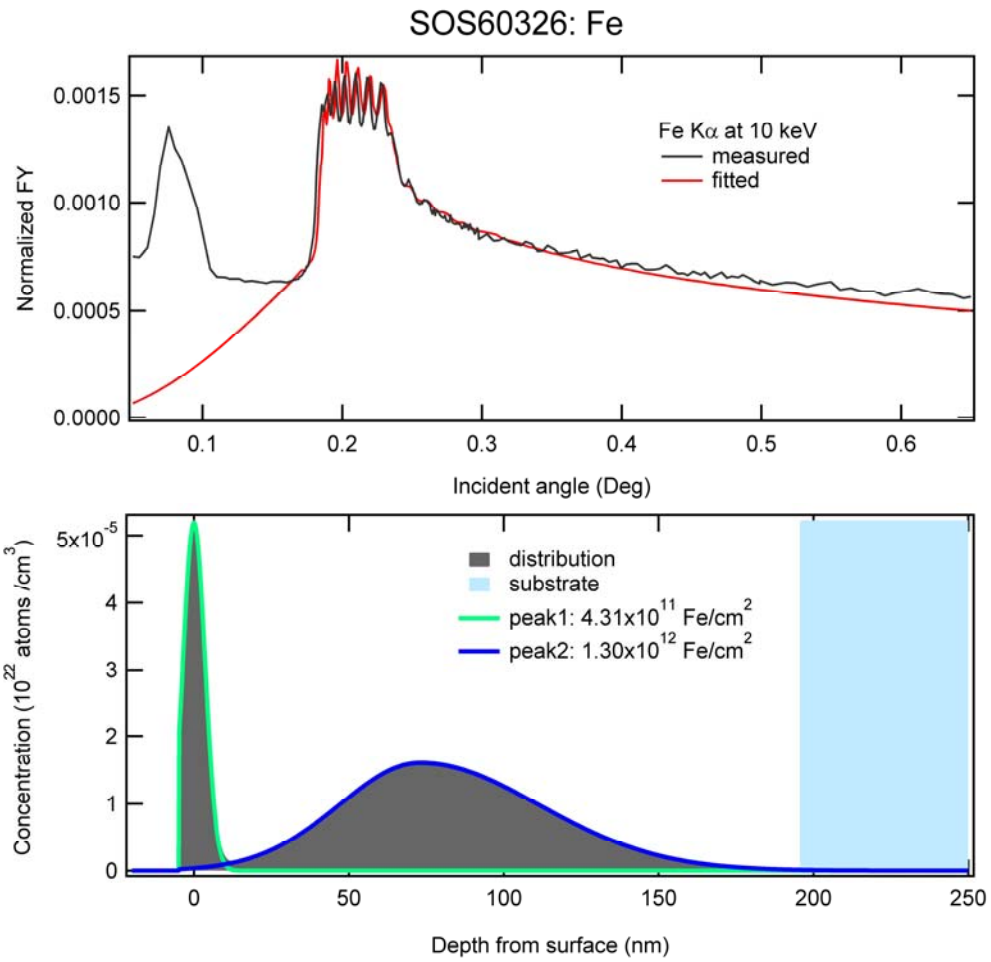

Figure 9: Top: Measured (black) and best-fit (red) fluorescence yield curves for Fe in flight sample SoS60326. The bottom plot shows the depth-dependent structure profile for Fe (gray area is the Fe distribution) corresponding to the red fit in the top plot. The fit was produced using two components, a Gaussian shaped surface component (Gaussian 1) and an asymmetric Gaussian shaped implant profile (Gaussian 2). The shape of the implant profile was constrained to be that measured by SIMS analysis for chromium (Fig. 2) as described in the text.

342
343 variance of the fit to the data with the majority of the uncertainty deriving from

344 deconvolution of the significant surface contamination component.

345 Fe fluorescence detected below ~0.18 deg in the yield profile (black curve in

346 Figure 9 top) suggests the presence of coarse, Fe-bearing, above-surface contamination

347 which was under-fit by the 1- dimensional model (red curve in Figure 9 top). This low-
348 angle misfit indicates that the Fe surface contamination determination (peak 1 in Figure 9
349 bottom inset) was underestimated but with negligible effect on the below-surface Fe
350 implant determination.

351 Solar wind fluence for Ni in SoS60326 was obtained in the same way as for Fe.
352 The top plot in Figure 10 shows the measured (black) and best-fit (red) fluorescence yield
353 curves for Ni. The bottom plot in Figure 10 shows the depth-dependent structure profile
354 for Fe corresponding to the red fit in Figure 10 top. The results for Ni yielded a surface-
355 correlated (contamination) concentration of $1.18 \pm 0.11 \times 10^{11}$ Ni atoms/cm^2 and $2.34 \pm$
356 0.22×10^{11} Ni atoms/cm^2, the latter being the solar wind implant. **The modeled depth**
357 **profile (Fig. 10 bottom) demonstrates that the measured Ni is distributed within the**
358 **silicon layer and not concentrated at the Si/sapphire interface.**

359 The Ni fluence determination was initially compromised by a detector artifact in
360 the XRF spectra; the pile-up (or "sum") peak from Ca Kα (i.e., "Ca Kα+Ca Kα")
361 produces an artifact peak at 7.38 keV which is unresolvable from Ni Kα (7.45 keV)
362 considering the ~ 0.15 keV energy resolution of the energy dispersive detector.
363 Consequently, SoS60326 received an additional cleaning procedure to reduce the initial
364 high level of Ca contamination on its surface. Interference from the Ca Kα pile-up can be
365 demonstrated to be negligible in the final dataset with the following argument. Since the
366 pile-up probability is independent of energy, the "Ca Kα+Ca Kα" intensity will be lower
367 than the "Ca Kα+Si Kα" (5.4 keV) intensity by the intensity ratio of Si Kα/Ca Kα. In the
368 0.1 deg XRF spectrum, an angle at which the Ca Kα intensity is maximum, Ca Kα = 1000
369 cts (counts in central MCA channel), Si Kα = 8×10^5 cts and the 5.4 keV peak

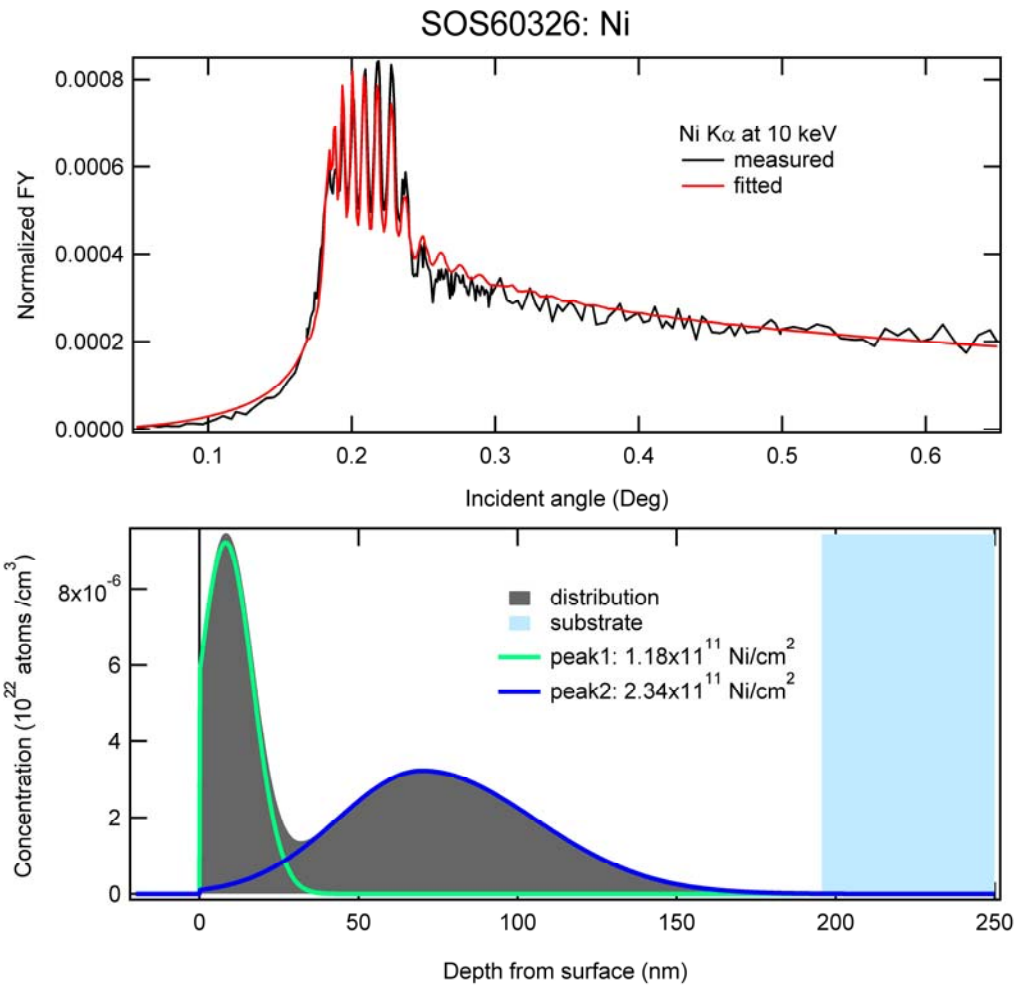

Fig. 10: Measured (black) and best-fit (red) fluorescence yield curves for Ni in flight sample SoS60326. The bottom plot shows the depth-dependent structure profile for Fe corresponding to the red fit in the top plot. The vertical line indicates the air-silicon interface. The fit was produced using two components, a Gaussian shaped surface component (Gaussian 1) and an asymmetric Gaussian shaped implant profile (Gaussian 2). The shape of the implant profile was constrained to be that measured by SIMS analysis for chromium (Fig. 2) as described in the text.

370
371 = 100 cts. Assuming the 5.4 keV peak is all pile-up (a worse-case scenario since a Cr Kα
372 contribution is likely) produces an upper limit for the "Ca Kα+Ca Kα" peak = 100/800 =
373 0.8 cts. Since all Ni Kα peaks in the SoS60326 spectra greatly exceed 1 ct, it is concluded
374 that the pile-up interference is negligible.

375 The inferred solar wind fluences for Fe and Ni assume the epitaxial Si layer of the
376 SoS collectors has negligible impurity concentrations of Fe and Ni. The flight criterion
377 was for impurity levels to be ≤ 10% (and ≤ 1% if possible) of the anticipated 2-yr solar
378 wind fluence for each element (Jurewicz et al. 2003; Burnett et al. 2003) although only a
379 subset of elements (including Fe and Ni) were verified to meet this criterion in at least
380 one member of the collector set but not necessarily in silicon-on-sapphire collectors

381 **3 Discussion**

382 Table 2 summarizes the fluence results from this work as well as other relevant
383 results in the literature. Previously, we reported (Kitts et al. 2009) a Fe fluence result for
384 a sapphire collector (50722) using a similar XSW experimental approach to that used
385 here except that a synthesized Fe-implanted Genesis spare was used as an external
386 standard, rather than using the internal reference method. That result, $1.6 \pm 0.4 \times 10^{12}$ Fe
387 atoms/cm^2, agrees well with the current result of $1.30 \pm 0.20 \times 10^{12}$ Fe atoms/cm^2; the
388 uncertainty is smaller in the latter because some sources of error are excluded when
389 utilizing the internal standard method. The agreement between the Fe fluences for the two
390 different collector materials (obtained in different experimental sessions) enhances the
391 reliability of these results. If the two fluence values are treated as independent, the
392 weighted mean is $1.36 \pm 0.18 \times 10^{12}$ Fe atoms/cm^2. This value agrees well with the SIMS
393 result of $1.41 \pm 0.08 \times 10^{12}$ Fe atoms/cm^2 (Jurewicz et al. 2011) for silicon-on-sapphire,
394 silicon, and diamond-like carbon collectors.

395 The pre-flight predicted Fe fluence was 1.7×10^{12} Fe atoms/cm^2 (Burnett et al.
396 2003) so the x-ray standing wave and SIMS results are in good agreement but about 20%

lower than this value. As discussed by Jurewicz et al. (2011), the low Fe fluence might be explained by ion fractionation effects in the solar wind. Commonly discussed processes include Coulomb drag, first ionization potential (FIP) effects and first ionization time (FIT). Spacecraft studies show no evidence of significant fractionation for elements with FIP < 9 eV such as Fe (Reisenfeld et al. 2007).

One way to test for fractionation effects is by comparing the concentrations of other elements. Jurewicz et al. (2011) specifically compared Fe with Mg from SIMS analyses, Mg is an element that has similar FIP near 8 eV but much lower FIT than Fe, and found no obvious fractionation.

Nickel is an element that has similar FIP and FIT to those of Fe and measured fluences might be useful in identifying fractionation processes. The measured Ni fluence of $2.34 \pm 0.22 \times 10^{11}$ Ni atoms/cm^2 is a factor of two higher than the expected fluence of $\sim 1 \times 10^{11}$ Ni atoms/cm^2 (Burnett et al. 2003). However, FIP of Ni is essentially equal to that of FIP of Fe (7.9 vs 7.6, respectively) and Fe doesn't appear to be fractionated from photospheric. FIT requires a model with accompanying uncertainties, whereas, FIP is an atomic constant.

Potential analytical reasons for over-estimation of the Ni solar wind fluence are discussed first. The possibility that the XRF sensitivity for Ni is too low can be ruled out by the facts that (1) Ni and Fe have very similar sensitivities and the Fe result is robust, and (2) the Ni concentration for the SoS implant is not overestimated. Another possibility is that the deconvolution of the surface-correlated (contamination) and implanted Ni has underestimated the amount of Ni in the former. This is highly unlikely based on the excellent fit obtained to the measured Ni fluorescence yield profile (Figure

10). A final possibility is that the Ni impurity concentration in the epitaxial silicon layer is comparable to the solar wind concentration. This might be ruled out because the selection criteria for the collector materials would preclude such high impurity levels, however, this possibility should be investigated further. There are a variety of potential contamination sources, including the post-flight cleaning process with ultra-pure water to remove Utah dust. However, the measured Fe fluences by multiple methods are reasonable so that any contamination mechanism would seem to require contamination by Ni and not Fe; not impossible but unlikely. The best way to evaluate the impurity level is through measurements on a SoS witness flag from the spacecraft. Unfortunately, the Utah impact prohibits the identification of such material. Next best is the analysis of SoS flight spares although the histories of these are not identical to those of the flight samples and a direct comparison may be difficult.

The measured Ni/Fe is 0.17 which is a factor of ~2.8 higher than spacecraft solar wind measurements, photosphere observations, and compositions of meteorites (Karrer et al. 2007). This result is surprising in light of the expected absence of significant solar wind fractionation of these two elements based on similar CD, FIT and FIP parameters. Specifically, it suggests that more work should be done in establishing the Ni concentration in the as-manufactured epitaxial silicon layers of the SoS collectors. If the Ni fluence result proves to be robust, one interpretation is that there exists temporally-variable Fe and Ni fractionation on the timescale of a year.

The internal reference method described here has the potential for providing solar wind fluence measurements of other elements, notably Cr and possibly Ca. Analyses of both of these elements are currently hindered by high Ca surface contamination. In

measuring Ca itself, this contamination leads to uncertainties in deconvolution of implanted Ca from the high surface-correlated components. For Cr, there is a potentially significant interference from the pile-up of "Si Kα+Ca Kα" at 5.43 keV which nearly exactly overlaps the Cr Kα peak at 5.41 keV. Improved cleaning procedures are likely to be needed to enable measurements on these elements.

4 Conclusions

X-ray standing wave fluorescence yield depth profiling was used to determine the solar wind implanted Fe and Ni fluences in a silicon-on-sapphire (SoS) Genesis collector (60326). An internal reference standardization method was developed based on fluorescence from Si and Al in the collector materials. Measured Fe fluence agreed well with that measured previously by us on a sapphire collector (50722) as well as SIMS results by Jurewicz et al. (2011). Measured Ni fluence was higher than expected by a factor of two; neither instrumental errors nor solar wind fractionation effects are considered significant perturbations to this value. Impurity Ni within the epitaxial Si layer remains a possibility that needs further investigation. If the measure Ni fluence is found to be robust, one interpretation is that there exists temporally-variable Fe and Ni fractionation on the timescale of a year.

5 Acknowledgements

The contributions of Kathy Kitts (the PI on the NASA grants supporting this project) are particularly acknowledged. Dr. Kitts was involved in the identifying appropriate samples for this work, collecting XSW data and reporting the initial results. The curatorial staff at Johnson Space Center is thanked for providing the flown samples

and the Genesis team for providing the implant standards. The manuscript was improved by the valuable reviews of A. Jurewicz and an anonymous reviewer. This research was supported by NASA Grants DDAP No. NNX07AG02G and SRLIDAP No. NNX07AL96G to Northern Illinois University (K. Kitts, PI), and NASA LARS grants NNX10AH05G to Loyola University Chicago (M. Schmeling, PI) and NNH09AM48I (I. Veryovkin, PI) to Argonne National Laboratory. This work was performed at GeoSoilEnviroCARS (The University of Chicago, Sector 13), Advanced Photon Source (APS), Argonne National Laboratory. GeoSoilEnviroCARS is supported by the National Science Foundation - Earth Sciences (EAR-1128799) and Department of Energy-GeoSciences (DE-FG02-94ER14466). This research used resources of the Advanced Photon Source, a U.S. Department of Energy (DOE) Office of Science User Facility operated for the DOE Office of Science by Argonne National Laboratory under Contract No. DE-AC02-06CH11357.

6 References

Becker, R. S., J. A. Golovchenko, and J. R. Patel, "X-Ray evanescent-wave absorption and emission," *Phys. Rev. Lett.* **50**,153-156 (1983).

Bedzyk, M. J., D. H. Bilderback, G. M. Bommarito, M. Caffrey, and J. S. Schildkraut, "X-ray standing waves: a molecular yardstick for biological membranes," *Science* **241**,1788-1791 (1988).

Bedzyk, M. J., G. M. Bommarito, and J. S. Schildkraut, "X-ray standing waves at a reflecting mirror surface," *Phys. Rev. Lett.* **62**,1376-1379 (1989).

487 Bloch, J. M., M. Sansone, F. Rondelez, D. G. Peiffer, P. Pincus, M. W. Kim and P. M.
488 Eisenberger, "Concentration profile of a dissolved polymer near the air-liquid
489 interface: X-Ray fluorescence study," *Phys. Rev. Lett.* **54**,1039-1042 (1985).
490 Burnett, D. S., "Solar composition from the Genesis Discovery Mission," *Proceedings of*
491 *the National Academy of Sciences* **108**, 19147-19151 (2011).
492 Burnett, D. S., "The Genesis solar wind sample return mission: Past, present, and future,"
493 *Meteoritics & Planetary Science* **48**, 2351-2370 (2013).
494 Burnett D. S., A. J. G. Jurewicz, D. S. Woolum, J. Wang, J. M. Paque, L. R. Nittler, K.
495 M. McKeegan, M. Humayun, R. Hervig, V. S. Heber, and Y. Guan Y., "Ion
496 implants as matrix-appropriate calibrators for geochemical ion probe analysis."
497 *Geostandards and Geoanalytical Research* **39**, 265-276 (2015).
498 Burnett, D. S., B. L. Barraclough, R. Bennett, M. Neugebauer, L. P. Oldham, C. N.
499 Sasaki, D. Sevilla, N. Smith, E. Stansvery, D. Sweetnam, and R. C. Wiens, "The
500 Genesis Discovery Mission: Return of solar matter to Earth," *Space Science*
501 *Reviews* **105**, 509-534 (2003).
502 Calaway, M. J., D. S. Burnett, M. C. Rodriguez, S. Sestak, J. H. Allton, and E. K.
503 Stansbery, E. K., "Decontamination uf Genesis array materials by UV ozone
504 cleaning (abstract 1338)," 38th Lunar and Planetary Science Conference (2007).
505 Chantler, C. T., "Detailed tabulation of atomic form factors, photoelectric absorption and
506 scattering cross section, and mass attenuation coefficients in the vicinity of
507 absorption edges in the soft x-ray (Z=30–36, Z=60–89, E=0.1 keV–10 keV),
508 addressing convergence issues of earlier work," *J. Phys. Chem. Ref. Data* **29**, 597-
509 1048, 2000.

510 Chantler, C. T., "Theoretical form factor, attenuation, and scattering tabulation for Z=1–
511 92 from E=1–10 eV to E=0.4–1.0 MeV," *J. Phys. Chem. Ref. Data* **24**, 71-643,
512 1995.
513 De Boer, D. K. G., "Glancing-incidence x-ray fluorescence of layered materials," *Phys.*
514 *Rev. B* **44**, 498-511 (1991).
515 Dev, B. N., A. K. Das, S. Dev, D. W. Schubert, M. Stamm, and G. Materlik G.,
516 "Resonance enhancement of x rays in layered materials: Application to surface
517 enrichment in polymer blends," *Phys. Rev. B* **61**, 8462-8468 (2000).
518 Elam, W. T., B. D. Ravel, and J. R. Sieber, "A new atomic database for x-ray
519 spectroscopic calculations," *Radiat. Phys. Chem* **63**, 121-128, 2002.
520 Ghose, S. K., B. N. Dev, and A. Gupta, "Resonance enhancement of X-rays and
521 fluorescence yield from marker layers in the thin films," *Phys. Rev. B* **64**,
522 233403(1-4) (2001).
523 Gupta, A., P. Rajput, and C. Meneghini, "Depth-resolved x-ray absorption fine structure
524 study of Fe/Si interfaces using x-ray standing waves," *Phys. Rev. B* **76**,195401(1-
525 8) (2007).
526 Heber V.S.,K. D. McKeegan, D. S. Burnett, J. Duprat, Y. Guan, A. J. G. Jurewicz, C. T.
527 Olinger, and S. P. Smith, "Accurate analysis of shallowly implanted solar wind
528 ions by SIMS backside depth profiling." *Chemical Geology* **390,** 61-73 (2014).
529 Jurewicz, A. J. G., D. S. Burnett, D. S. Woolum, K. D. McKeegan, V. Heber, Y. Guan,
530 M. Humayun, and R. Hervig, "Solar-wind Fe/Mg and a comparison with CI
531 chondrites (abstract 1917)," 42nd Lunar and Planetary Science Conference (2011).

532 Jurewicz, A. J. G., D. S. Burnett, R. C. Wiens, T. A. Friedmann, C. C. Hays, R. J.
533 Hohlfelder, K. Nishiizumi, J. A. Stone, D. S. Woolum, R. Becker, A. Butterworth,
534 A. J. Campbell, M. Ebihara, I. A. Franchi, V. Heber, C. M. Hohenberg, M.
535 Humayun, K. D. McKeegan, K. McNamara, A. Meshik, R. O. Pepin, D. Schlutter,
536 and R. Wieler, "The Genesis solar-wind collector materials," *Space Science*
537 *Reviews* **105**, 535-560 (2003).
538 Karrer R., P. Bochsler, C. Giammanco, F. M. Ipavich, J. A. Paquette, and P. Wurz,
539 "Nickel isotopic composition and nickel/iron ratio in the solar wind: Results from
540 SOHO/CELIAS/MTOF," *Space Sci. Rev.* **130**, 317-321, 2007.
541 Kitts, K., Y. Choi, P. J. Eng, S. K. Ghose, S. R. Sutton, and B. Rout, "Application of
542 grazing incidence x-ray fluorescence technique to discriminate and quantify
543 implanted solar wind," *J. Appl. Phys.* **105**, 064905(1-3) (2009).
544 Krause, M. O. and J. H. Oliver J. H., "Natural widths of atomic K and L levels, Ka X-ray
545 lines and several KLL Auger lines," *J. Phys. Chem.* **8**, 329-338 (1979).
546 Krause, M. O., "Atomic radiative and radiationless yields for K and L shells," *J. Phys.*
547 *Chem. Ref. Data* **8**, 307-327, 1979.
548 Lee, D. R., A. Hagman, X. Li, S. Narayanan, J. Wang, and K. R. Shull, "Perturbation to
549 the resonance modes by gold nanoparticles in a thin-film-based x-ray waveguide,"
550 *Appl. Phys. Lett.* **88**, 153101(1-3) (2006).
551 McMaster, W. H., N. Kerr Del Grande, J. H. Mallett, and J. H. Hubbell, "Compilation of
552 x-ray cross sections," *Lawrence Radiation Laboratory Report UCRL-5017*
553 (National Bureau of Standards, Springfield, Virginia), 1969.

McNamara, K. M., and E. K. Stansbery E. K., "Analysis of molecular contamination on Genesis collectors through spectroscopic ellipsometry (abstract 2402)," 36th Lunar and Planetary Science Conference (2005).

Parratt, L. G., "Surface studies of solids by total reflection of x-rays," *Phys. Rev.* **95**, 359-369 (1954).

Reisenfeld, D. B., D. S. Burnett, R. H. Becker, A. G. Grimberg, S. Heber, C. M. Hohenberg, A. J. G. Jurewicz, A. Meshik, R. O. Pepin, J. M. Raines, D. J. Schlutter, R. Wieler, R. C. Wiens, and T. H. Zurbuchen, "Elemental abundances of the bulk solar wind: Analyses from Genesis and ACE," *Space Science Reviews* **130**, 79-86, 2007.

Sigmund, P., and A. Gras-Marti, "Distortion of depth profiles during sputtering: I. General description of collisional mixing," *Nuclear Instruments and Methods* **168**, 389-394 (2001).

Templeton, A. S., T. P. Trainor, S. J. Traina, A. M. Spormann, and G. E. Brown, Jr., "Pb(II) distributions at biofilm–metal oxide interfaces," *Proceedings of the National Academy of Sciences* **98**,11897-11902 (2001).

Tiwari, M. K., G. M. Bhalerao, M. Babu, A. K. Sinha, and C. Mukherjee, "Investigation of metal nanoparticles on a Si surface using an X-ray standing wave field," *J. Appl. Phys.* **103**, 054311(1–6) (2008).

Trainor, T. P., A. S. Templeton, and P. J. Eng, "Structure and reactivity of environmental interfaces: Application of grazing angle x-ray spectroscopy and long-period x-ray standing waves," *J. Electron. Spectrosc. Relat. Phenom.* **150**, 66-85 (2006).

576 Veryovkin, I. V., C. E. Tripa, A. V. Zinovev, B. V. King, M. J. Pellin, and D. S. Burnett,
577 "RIMS analysis of Ca and Cr in Genesis solar wind collectors," *Surface and*
578 *Interface Analysis* **43(1-2)**, 467-469 (2011).
579 Wang, J., M. J. Bedzyk, and M. Caffrey, "Resonance-enhanced x-rays in thin films: A
580 structure probe for membranes and surface layers," *Science* **258**, 775-778 (1992).
581

582 **Table 1:** Tabulated values for photo-electric cross-sections (in Barns/atoms) and
583 fluorescence yield (unitless). C_{Int} is the product of the two. C_{Ext} is the product of the
584 transmission ratios from the sample surface through the fluorescence detector for each
585 Kα radiation.
586

	Al	Si	Cr	Fe
$\sigma_{photo\text{-}e}$(7.6 keV)	2615.0	3546.5	25213.7	31805.2
ω_K	0.039	0.05	0.275	0.34
C_{Int}	102.0	177.3	10813.8	6933.8
C_{Ext}	0.004822	0.03303	0.8802	0.9263

587

588 **Table 2:** Summary of solar wind fluence results for Fe and Ni

	Sample number	**Fe fluences (atoms/cm^2)**	**Ni fluences (atoms/cm^2)**
X-ray standing waves#			
Silicon-on-sapphire	60326	$1.30 \pm 0.10 \times 10^{12}$	$2.34 \pm 0.22 \times 10^{11}$
Sapphire*	50722	$1.6 \pm 0.4 \times 10^{12}$	NA
Two-collector mean		$1.36 \pm 0.18 \times 10^{12}$	NA
Ni/Fe		0.17	
SIMS^		$1.41 \pm 0.08 \times 10^{12}$	NA
Predicted fluences$		1.7×10^{12}	1.0×10^{11}

This work

* Kitts et al. 2009

^ Jurewicz et al. 2011

$ Burnett et al. 2003

NA = not available

589